

The nucleation of Mo-rich Laves phase particles adjacent to $M_{23}C_6$ micrograin boundary carbides in 12% Cr tempered martensite ferritic steels

M.I. Isik,^a A. Kostka,^{a,b,*} V.A. Yardley,^b K.G. Pradeep,^{a,c} M.J. Duarte,^a P.P. Choi,^a D. Raabe^a and G. Eggeler^{a,b}

^aMax-Planck-Institut für Eisenforschung GmbH, 40237 Düsseldorf, Germany

^bInstitut für Werkstoffe, Ruhr-Universität Bochum, 44801 Bochum, Germany

^cLehrstuhl für Werkstoffchemie, RWTH Aachen University, 52074 Aachen, Germany

Received 25 October 2014; revised 14 January 2015; accepted 17 January 2015

Abstract—We study the nucleation of Mo-rich Laves phase particles during aging and creep of 12 wt.% Cr tempered martensite ferritic steels (TMFS). Recently, in Isik et al. (2014) we reported that Laves phase particles tend to form at micrograin boundaries of TMFSs after Mo and Si had segregated from the ferritic matrix to these internal interfaces. In the present work, we employ transmission electron microscopy (TEM) and atom probe tomography (APT) to study the formation of Laves phase particles. We investigate the preference of Laves phase particles to nucleate next to $M_{23}C_6$ micrograin boundary carbides. Our results suggest that this joint precipitation effect is due to the combined segregation of Mo and Si from the matrix to the micrograin boundaries and Si and P enrichment around the growing carbides.
Published by Elsevier Ltd. on behalf of Acta Materialia Inc.

Keywords: Tempered martensite ferritic steels; Laves phase; $M_{23}C_6$ carbides; Transmission electron microscopy (TEM); Atom probe tomography (APT)

1. Introduction

Tempered martensite ferritic steels (TMFSs) are often used for critical components in fossil-fired power plants where they operate in the creep range, meaning that they have to withstand mechanical loads at temperatures up to 650 °C [1–9]. The heat treatment of TMFSs consists of austenitization (~1050 °C, ~0.5 h) and tempering (~750 °C, 2–4 h) both followed by air cooling [10,11]. The microstructure evolution during this type of heat treatment has been described in the literature [12–21]. The main feature, however, is a high density of hierarchically organized internal interfaces with different, yet characteristic, crystallographic and chemical properties [22].

In TMFSs, both high- and low-angle grain boundaries are present. High-angle grain boundaries include prior austenite grain boundaries, prior block boundaries and prior lath boundaries. After tempering all these interfaces constitute high-angle ferrite boundaries. The high dislocation density, which is normally associated with the martensitic transformation, can partly recover during tempering, giving rise to the formation of low-angle grain boundaries. These subgrain boundaries and the prior lath boundaries form the

characteristic ultra-fine grained microstructure of TMFSs [9,23,24].

A schematic illustration of such tempered martensite ferritic microstructure, typical for 9–12 wt.% Cr steels, is given in Fig. 1 [24]. The microstructure mainly consists of ultra-fine grains, pertaining to a group of small, i.e. μm -sized ferritic crystals [25–27]. These grains, being ~2 μm long and ~0.5 μm wide, are simply referred to as ‘micrograins’. In addition, highly dispersed boundary-pinning carbides are present. Two types of carbides can be distinguished, namely, large and small carbides. The large, bulky carbides have a size of ~500 nm while the small ones are ~50 nm in size and have elongated shapes following the micrograin boundaries [9]. A large number fraction of carbides precipitate on or very close to micrograin boundaries [27,28].

Creep mechanisms of TMFSs have been studied extensively over the last three decades [29–34] specifically with respect to the shape of the creep curves, the stress and temperature dependence of the creep rate [25,27,35], the role of alloying elements [6,36–38], the influence of heat treatment on creep behavior [39,40] and the evolution of the microstructure during creep [12,26,41,42]. It has been found that the initial high density of dislocations decreases during high temperature exposure and creep [7,14,28,39,43,44]. It was also shown that the chemical composition of the $M_{23}C_6$ carbides changes according to their temperature dependent local thermodynamic equilibrium. They also

* Corresponding author at: Max-Planck-Institut für Eisenforschung GmbH, 40237 Düsseldorf, Germany; e-mail: a.kostka@mpie.de

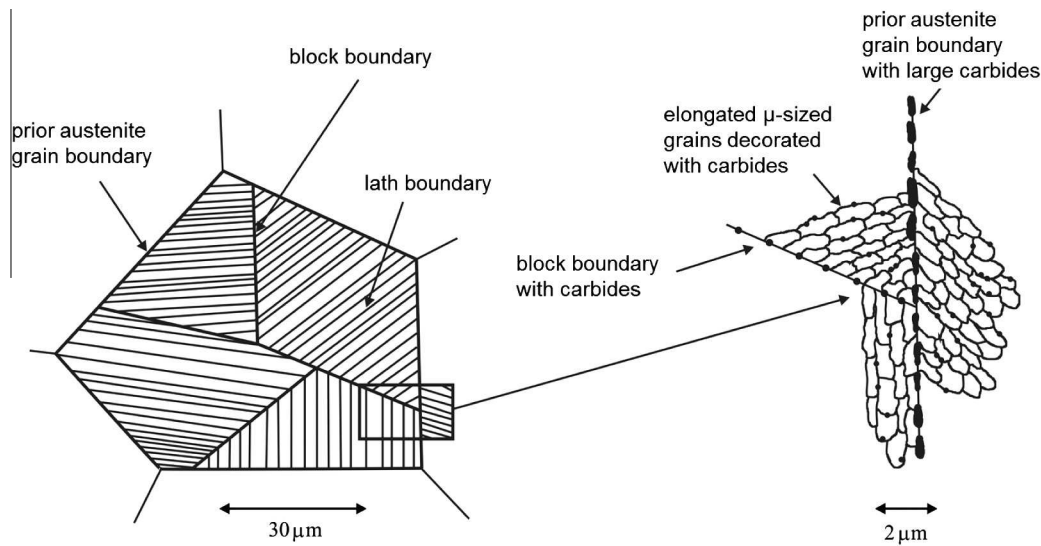


Fig. 1. Schematic illustration of 9–12% Cr tempered martensite ferritic steel microstructure [24].

Table 1. Chemical composition of alloy S and alloy L obtained by inductively coupled plasma-optic emission spectroscopy (ICP-OES) and infrared absorption analyses.

	C	Si	Mn	P	S	Cr	Mo	V	Al	Ni
Alloy S wt.%	0.2	0.15	0.61	0.01	0.01	11.7	1.13	0.25	0.01	0.65
at.%	0.9	0.29	0.61	0.02	0.02	12.4	0.65	0.27	0.02	0.61
Alloy L wt.%	0.2	0.16	0.58	0.01	0.01	11.7	0.84	0.25	0.01	0.68
at.%	0.9	0.31	0.58	0.02	0.02	12.4	0.48	0.27	0.02	0.64

undergo coarsening through Ostwald ripening [17,28,45,46]. Other precipitates of type MX, especially VC, were shown to be stable at temperatures below 600 °C [28,42,47,48].

In this context, software tools such as MatCalc [49,50] serve to predict the stability of the different phases that form in these complex steels. The compositions of two TMFSs, referred to as alloys S (high in Mo, 1.13 wt.%) and L (low in Mo, 0.84 wt.%), are given in Table 1 (determined by inductively coupled plasma-optic emission spectroscopy (ICP-OES) and infrared absorption analyses). Fig. 2 shows the thermodynamic predictions obtained by MatCalc for the two alloy compositions. Two quasi binary sections of phase diagrams with increasing Mo and Si contents are shown in Fig. 2a and b, where the alloys S and L are represented by squares and circles, respectively. Fig. 2a shows that a solubility line defines the boundary between a two-phase (ferrite and $M_{23}C_6$) and a three-phase region (ferrite, $M_{23}C_6$ and Laves phase). Accordingly, a certain minimum amount of Mo is required to stabilize the Laves phase. This amount of Mo increases with increasing temperature. At 550 °C, the alloy L is located exactly on this solubility line, while the alloy S with its higher Mo content is fully embedded in the three phase region. We have recently shown that segregation of Mo to micrograin boundaries in TMFSs can promote the formation of the Laves phase [1]. Fig. 2b shows that there is also a minimum amount of Si required for the stabilization of the Laves phase. MatCalc calculations also reveal that in equilibrium $M_{23}C_6$ carbides do not contain Si (predicted phase compositions are given in Table 2). From the thermodynamic

phase diagram predictions presented in Fig. 2, we expect the presence of Laves phase particles in alloy S. However, neither in alloy L nor in alloy S Laves phase particles were detected in the initial state (after heat treatment prior to aging/creep). However, during aging and creep, Laves phase particles have been observed to form as also has been reported previously [15,25,28,41,42,51–54]. Aghajani et al. [28] showed that during creep at 550 °C and 120 MPa, Laves phase particles form with a specific composition, characterized by ~7 at.% Si. This composition does not change during aging (550 °C) or creep (550 °C, 120 MPa). It was also reported that these Laves phase particles nucleate continuously during creep and that a duration of 139,971 h at 550 °C is not sufficient to establish thermodynamic equilibrium [28]. It has been suggested that the slow and continuous nucleation of Laves phase particles is related to slow Si diffusion [55]. TMFSs generally contain small amounts of Si (up to 2 at.%, e.g. [5,6,9,25,51,56–59]). In Isik et al. [1], we showed experimentally that the segregation of Mo and Si to micrograin boundaries precedes the nucleation of Laves phase particles at micrograin boundaries. This is in good agreement with the conclusions of Hosoi et al. [51], who showed that lower Si concentrations in TMFs resulted in longer elevated temperature exposure times required for Laves phase nucleation. Recently, we showed that the Laves phase particles nucleate at micrograin boundaries (with increased Si content), adjacent to $M_{23}C_6$ carbides during high temperature exposure and creep [1]. We revealed the role of Si in the Laves phase nucleation process. It remains to be clarified why Laves phase particles nucleate close to $M_{23}C_6$ micrograin

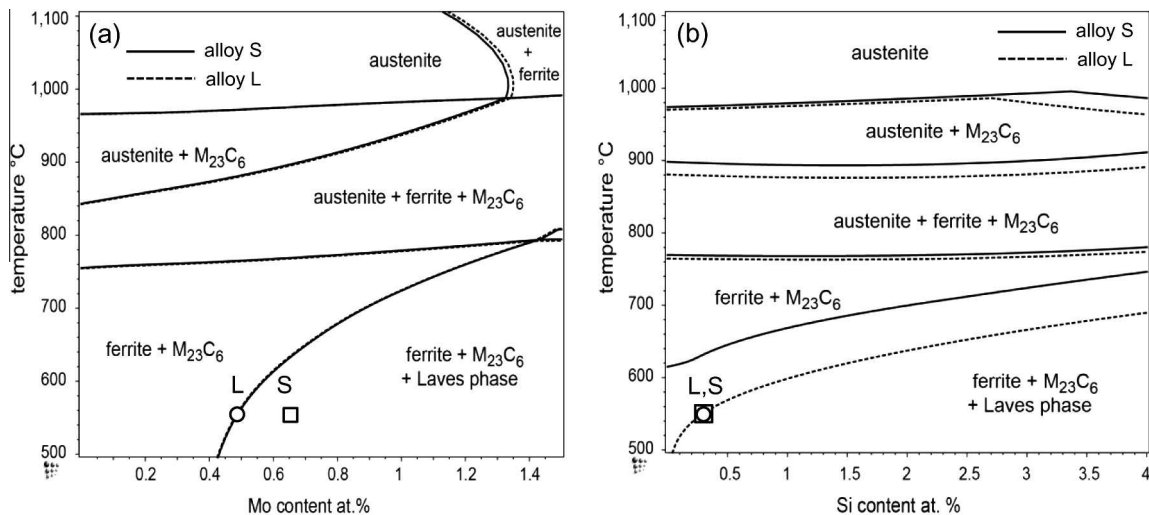


Fig. 2. Pseudobinary sections of phase diagrams with increasing (a) Mo and (b) Si content (MatCalc with database mc_fe_v2.040.tdb) [49,50]. Alloy S is high in Mo, 1.13 wt.%, and alloy L is low in Mo, 0.84 wt.%, see Table 1.

Table 2. MatCalc prediction of the chemical composition of the stable phases at 550 °C. Values are given in at.%.

	Mo	Fe	Cr	Si	C
<i>Alloy S</i>					
M ₂₃ C ₆	9	6.5	63.6	–	20.7
Laves phase	33	48.9	8.3	8.9	–
Ferrite	0.09	88	10	0.26	2.23 × 10 ^{−3}
<i>Alloy L</i>					
M ₂₃ C ₆	9	6.6	63.6	–	20.7
Laves phase	33.1	48.7	8.2	9.2	–
Ferrite	0.09	88	10	0.33	2.26 × 10 ^{−3}

Table 3. Material states of X20CrMoV12–1 specimens. Aging: 550 °C. Creep: 550 °C, 120 MPa.

Ref.	State	Strain (%)	Time (h)
<i>Alloy S</i>			
S0	Initial	0	0
S2b	Crept	0.4	2400
<i>Alloy L</i>			
L1a	Aged	–	12,456
L2a	Aged	–	51,072
L3a	Aged	–	81,984
L3b	Crept	1.6	81,984

boundary carbides. In the present work, we use transmission electron microscopy (TEM) and atom probe tomography (APT) to explain why M₂₃C₆ carbides promote the nucleation of Laves phase particles on micrograin boundaries in TMFSs.

2. Materials and methods

In the present study, two TMFSs were investigated, referred to as alloys S and L. The alloy S is richer in Mo, 1.13 wt.%, compared to the alloy L which has a Mo content of 0.84 wt.% as shown in Table 1. The investigated material

was supplied by Salzgitter Mannesmann Research Center containing close to 12% Cr. A two-stage heat treatment procedure was applied, consisting of austenitization at 1050 °C for 0.5 h and tempering at 770 °C for 2 h, both followed by air cooling. Interrupted creep tests were carried out at 120 MPa and 550 ± 1 °C. Table 3 shows the material states that were investigated in the present study. Aged material states were obtained from the undeformed sample heads of the creep specimens. While we cannot exclude the presence of moderate levels of stress in the thread sections of creep specimens, no significant strain accumulation takes place in those regions [24,53]. The crept material states (S2b and L3b in Table 3) were taken from the gauge lengths of the corresponding creep specimens (no necking). TEM foils were prepared by mechanical polishing 3 mm disks to a thickness of 80 μm followed by double-jet electro-polishing. The electrolyte consisted of 95% acetic and 5% perchloric acid. Electro-polishing was performed at 15 °C using applied voltages of 41 V (for alloy S) and 58 V (for alloy L). Transmission electron microscopy (TEM) was carried out using a Jeol JEM-2200FS at 200 kV. The TEM was equipped with an energy dispersive X-ray analysis system (EDX). Only Fe, Cr and Mo were considered during EDX analysis. Specimens for atom probe tomography (APT) were prepared from electropolished TEM disks using focused-ion-beam (FIB, FEI Helios NanoLab 600) micro-machining in combination with a lift-out method. This APT sample preparation procedure has been previously described elsewhere [60–62]. Local electrode atom probe (LEAP 3000× HR, Cameca Instr.) measurements were performed for the initial state material in voltage mode (pulse fraction of 15%) and the crept state material in laser mode (0.4 nJ pulses), both at a specimen temperature of 60 K. A pulse repetition rate of 200 kHz was applied achieving a maximum detection rate of 1.3%. APT data post-processing was performed using the IVAS™ 3.6.6 software [63,64]. Concentration profiles were obtained as proximity histograms from specific interfaces with a width of 1 nm. The obtained chemical compositions of the studied phases reveal small differences when quantitative EDX data (Table 4) are compared to APT data (Tables 5 and 6). These differences are related to the different physical

Table 4. TEM EDX analyses of the phases after 2400 h creep (material state S2b in Table 3) from Fig. 4 (relative at.% of Mo, Fe and Cr).

	Mo	Fe	Cr
Laves phase	32.5 ± 1.3	$53.2 \pm .5$	$14.3 \pm .3$
Ferrite	$0.5 \pm .2$	$88.2 \pm .3$	$11.3 \pm .1$
$M_{23}C_6$	$4.8 \pm .3$	$28.3 \pm .2$	$66.9 \pm .3$

principles of the applied techniques and their sensitivity to the analyzed elements as well as to the sample preparation procedure.

Thermodynamic calculations were performed using the MatCalc software (employing the mc-fe-v2.040.tdb database) [49,50] which is based on the CALPHAD method. The CALPHAD method uses fitted model approximations for the Gibbs energies for specific phases [65–70]. In our calculations ferrite, austenite, liquid, cementite, $M_{23}C_6$, M_6C , M_7C_3 , MnS, Laves phase, Z-phase and sigma phases were considered. In a first order approximation, the nitrogen content of the steel was neglected and thus the formation of precipitates such as MX carbonitrides was excluded.

3. Results

3.1. TEM results

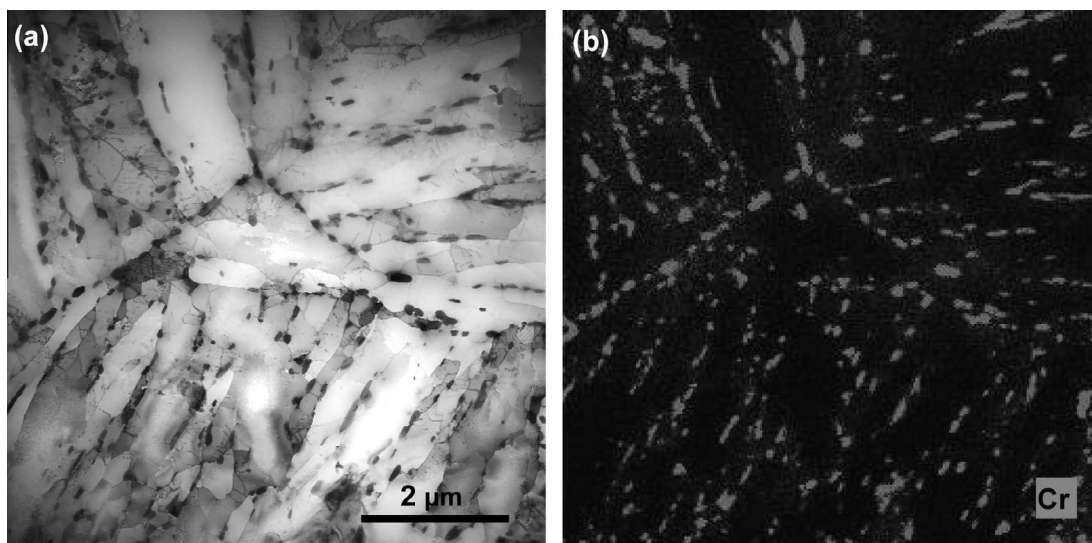
In both alloys investigated, no Laves phase was detected prior to aging and creep. A typical micrograin structure of the initial state material is presented in Fig. 3. Fig. 3a shows a scanning TEM image and Fig. 3b presents a Cr EDX map of the corresponding region. Carbides are rich in Cr (Cr is shown in gray in Fig. 3b), and hence, plotting Cr data allows us to locate carbides. In the early stages of aging and creep, Laves phase particles nucleate as rods which eventually evolve into a bulky shape during high temperature exposure [1]. An example of a rod-like Laves phase particle (width: ~ 10 nm; length: ~ 70 nm) formed during creep is shown in the TEM micrographs of Fig. 4a (STEM bright field micrograph) and b (STEM high angle annular dark field, HAADF, image). The elongated Laves phase particle marks a micrograin boundary which connects two $M_{23}C_6$ carbides. The corresponding energy dispersive X-ray (EDX) map in Fig. 4c was obtained by

Table 5. APT chemical compositions (at.%) of the phases shown in Fig. 7 (material state S0 in Table 3). The balance corresponds to the omitted elements.

	Mo	Fe	Cr	Si	C
Ferrite	$0.29 \pm .05$	$88.7 \pm .2$	$9.4 \pm .2$	$0.31 \pm .03$	$0.02 \pm .01$
$M_{23}C_6$	$3.7 \pm .2$	$22.9 \pm .4$	$55.4 \pm .5$	$0.005 \pm .002$	$15.8 \pm .3$

Table 6. APT measured chemical compositions (at.%) of the phases shown in Fig. 9 (material state L3b in Table 3). The balance corresponds to the omitted elements.

	Mo	Fe	Cr	Si	C
Laves phase	$30.1 \pm .5$	$42.3 \pm .5$	$13.2 \pm .3$	$10.2 \pm .3$	$0.13 \pm .01$
Ferrite	$0.17 \pm .04$	$88.9 \pm .2$	$9.3 \pm .2$	$0.31 \pm .03$	$0.06 \pm .02$
$M_{23}C_6$	$3.6 \pm .2$	$18.9 \pm .4$	$56.4 \pm .5$	<0.005	$18.8 \pm .3$

**Fig. 3.** Tempered martensite ferritic microstructure (material state S0 in Table 3). (a) STEM bright field. (b) Corresponding Cr (displayed in gray color) EDX map showing location of carbides.

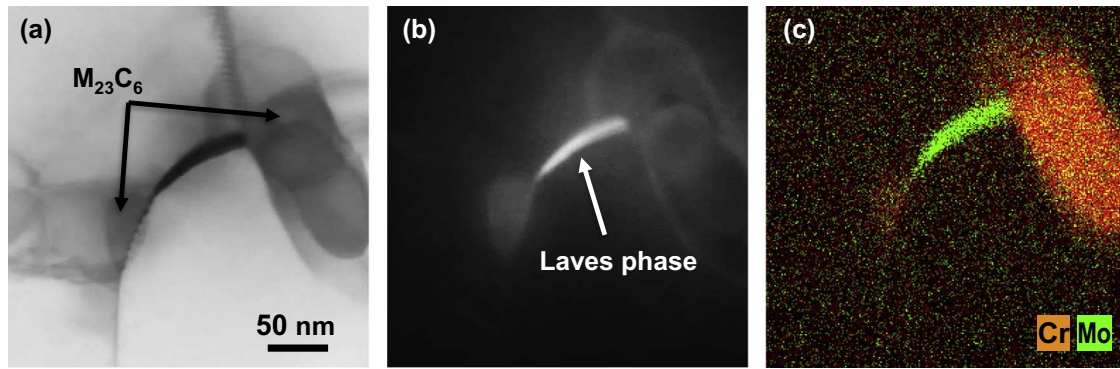


Fig. 4. Evolution of the microstructure after creep for 2400 h (material state S2b in Table 3). (a) STEM bright field image showing a small Laves phase along the grain boundary. (b) STEM HAADF image showing a Laves phase particle bridging two carbides. (c) Corresponding EDX map of Cr (orange, highlighting carbides) and Mo (green, denoting a Laves phase).

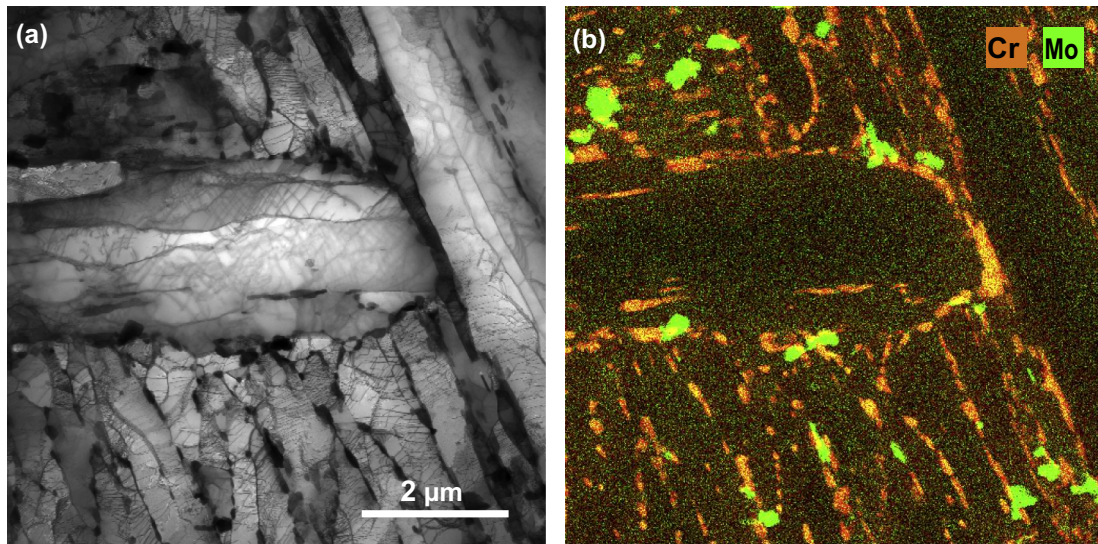


Fig. 5. Overview of the microstructure after long-term aging (material state L3a in Table 3). (a) STEM bright field image showing the micrograin structure and several precipitates. (b) EDX map of Cr (orange, highlighting carbides) and Mo (green, highlighting Laves phase particles).

merging color coded information of Cr (orange, highlighting $M_{23}C_6$) and Mo (green, highlighting Laves phase). The concentrations of the major elements in the phases shown in Fig. 4 are given in Table 4. Fig. 5 shows lower magnification overview micrographs of the microstructure after long-term high temperature exposure (material state L3a in Table 3). A STEM bright field image and the corresponding EDX map are shown accordingly in Fig. 5a and b. As can be seen from Fig. 5b, Laves phase particles (green) are mostly located at micrograin boundaries in close proximity to $M_{23}C_6$ carbides (orange). Fig. 6 shows average TEM EDX results together with the mean deviation from the mean value (error bars) which were obtained for two groups of 50 carbides each. The first group, referred to as “adjacent” in Fig. 6, consists of carbides in direct contact with Laves phase particles. The second group of carbides had no connection with Laves phase particles and is referred to as “isolated”. The EDX results in Fig. 6 clearly reveal that both groups of carbides contain nearly identical levels of Mo, Fe and Cr (material state: L2a in Table 3).

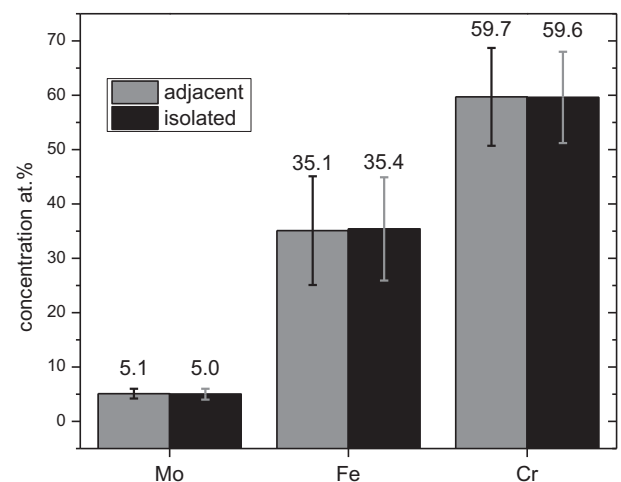


Fig. 6. TEM EDX results of selected element concentrations of $M_{23}C_6$ carbides in adjacent and isolated positions with respect to Laves phase particles (material state L2a in Table 3).

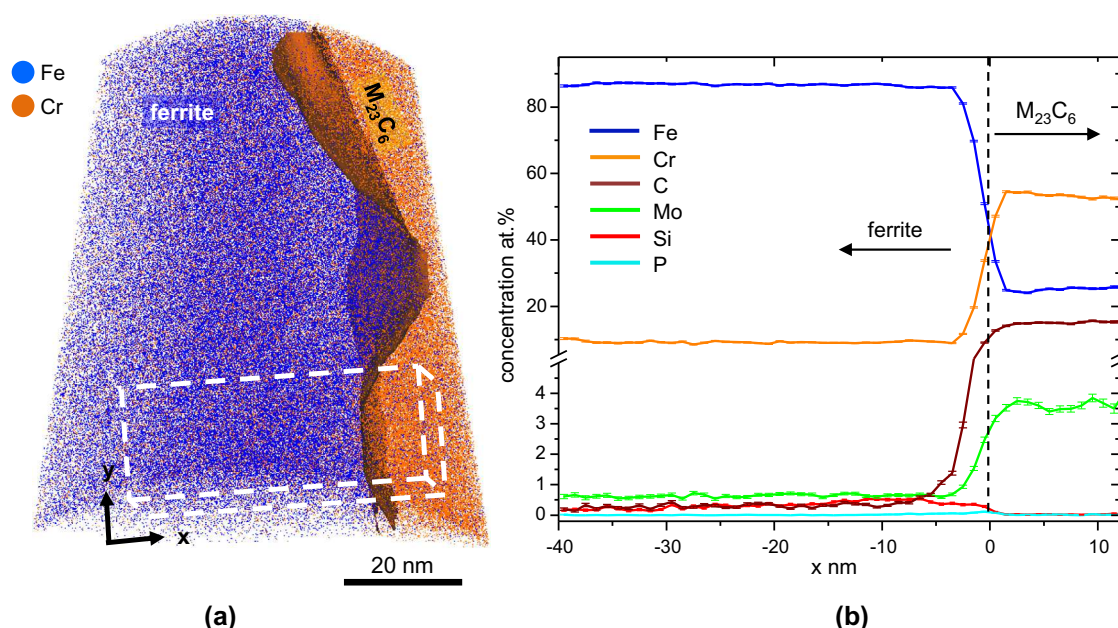


Fig. 7. APT reconstruction showing (a) the distribution of Fe (blue) and Cr (orange) atoms in initial state specimen (material state S0 in Table 3). Isoconcentration surface of 40 at.% Cr + C is plotted to highlight the interface between two phases. (b) Concentration profiles of selected elements across the marked section of the ferrite/ $M_{23}C_6$ carbide interface.

3.2. Atom probe analysis

We use APT to measure the local chemistry and elemental distribution at the carbide/ferrite interfaces as shown in Fig. 7. An $M_{23}C_6$ carbide (orange) in the right part of Fig. 7a is in contact with a ferritic matrix region (violet) for the material state S0 in Table 3. The orange color is associated with Cr atoms while Fe atoms appear in blue. The mixture of Fe and Cr atoms creates the violet color of the ferrite in Fig. 7a. The interface between carbide and ferrite is not perfectly flat and is therefore visualized using an isoconcentration surface of 40 at.% Cr + C. The concentrations of the major alloying elements present in the two phases are given in Table 5. About 4 at.% Mo is present in $M_{23}C_6$ carbide which is close to the EDX data given in Table 4 and Fig. 6 (note that C was not considered in our EDX measurements). Fig. 7a also shows the projection of an elongated cuboidal space of $(30 \times 30 \times 60 \text{ nm}^3)$ where local concentrations were evaluated along the space coordinate x . The concentration profiles taken along the x axis are plotted in Fig. 7b. A strong decrease in the Fe concentration can be observed as we move from the ferrite into the $M_{23}C_6$ carbide. This is accompanied by an increase of Cr (no depletion at the interface detected), Mo (no enrichment at the interface detected) and C. To better visualize the small P and Si contributions, the mentioned sub-volume was extracted and plotted in Fig. 8a. Si and P atoms are displayed as red and cyan spheres, while Cr and Fe atoms are shown as orange and blue dots, respectively. In the ferrite matrix, an enrichment of Si next to the $M_{23}C_6$ carbide interface can be seen. The corresponding concentration profiles of Si and P atoms are presented in Fig. 8b. From the data plotted, we can conclude that the Si concentration in $M_{23}C_6$ carbide is very low (~ 0.005 at.% Si as given in Table 5). In about 20 nm distance from the $M_{23}C_6$ interface toward ferrite, the Si concentration is above ~ 0.5 at.% while it decreases to 0.2 at.% as we move away from the carbide. Fig. 8b also

presents experimental evidence for enrichment of P at the ferrite/carbide interface.

Fig. 9 shows the spatial distributions of Fe (blue), Cr (orange) and Mo (green) atoms in a specimen after long-term creep (material state L3b in Table 3). Violet, orange and green regions represent ferrite, $M_{23}C_6$ carbide and Laves phase, respectively. The chemical compositions of all the corresponding phases are listed in Table 6. Elemental concentration profiles taken along the reference lines (white arrows in Fig. 9 numbered 1, 2 and 3) are plotted in Fig. 10. Fig. 10a displays the concentration profile of the selected elements along the ferrite/ $M_{23}C_6$ interface (measured along arrow 1 in Fig. 9). The concentrations of Si and P are very low and therefore, the Si and P distributions are plotted separately with a higher concentration resolution in Fig. 10b. It can be seen that the Si concentration drops sharply from about ~ 0.4 at.% at the interface toward ~ 0.01 at.% in the carbide. Also, a sharp P peak at the ferrite/carbide interface is detected. The concentration of P at the ferrite/carbide interface was about ~ 0.5 at.%. Similar to the initial state material (Fig. 8), the Si concentration of the ferrite matrix is about ~ 0.3 at.%. Fig. 10c shows the concentration profiles measured across the Laves phase/ferrite interface (along arrow 2 in Fig. 9). Table 6 shows that the Cr content in the Laves phase (~ 13.2 at.%) is higher than in ferrite (~ 9.3 at.%). The results shown in Fig. 10c and Table 6 suggest that the Laves phase particles observed here are of type $(Fe, Cr, Si)_2Mo$ containing about 30 at.% Mo, 42 at.% Fe, 13 at.% Cr and 10 at.% Si. The concentration profiles across the Laves phase/ $M_{23}C_6$ carbide interface (along arrow 3 in Fig. 9) are shown in Fig. 10d. The results reveal that the Mo content in $M_{23}C_6$ carbide is close to 4 at.%. Fig. 11 displays the spatial distribution of Cr (orange) and P (cyan) atoms. All the phases captured in the APT data set are marked in Fig. 11. They contain the following at.% of P: ~ 1.31 (Laves phase), ~ 0.01 (ferrite) and ~ 0.01 ($M_{23}C_6$ carbide). The elevated P level in the Laves phase and the

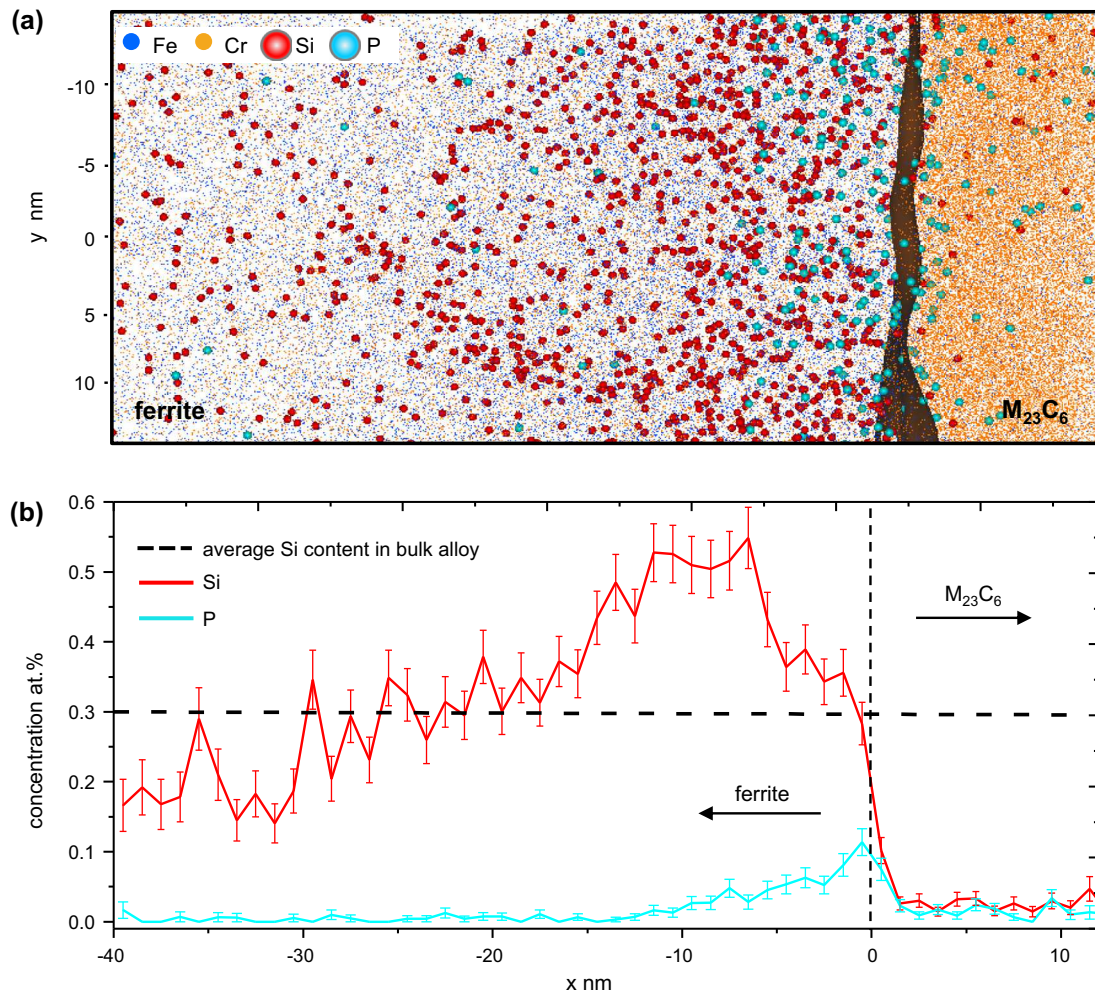


Fig. 8. APT data obtained from the reference volume in Fig. 7a. (a) Reconstruction showing the distribution of Si (red spheres), P (cyan spheres), Cr (orange dots) and Fe (blue dots) atoms in ferrite and $M_{23}C_6$ carbide. The ferrite/carbide interface is highlighted by an isoconcentration surface of 40 at.% Cr + C. (b) Concentration profile of Si and P along x axis.

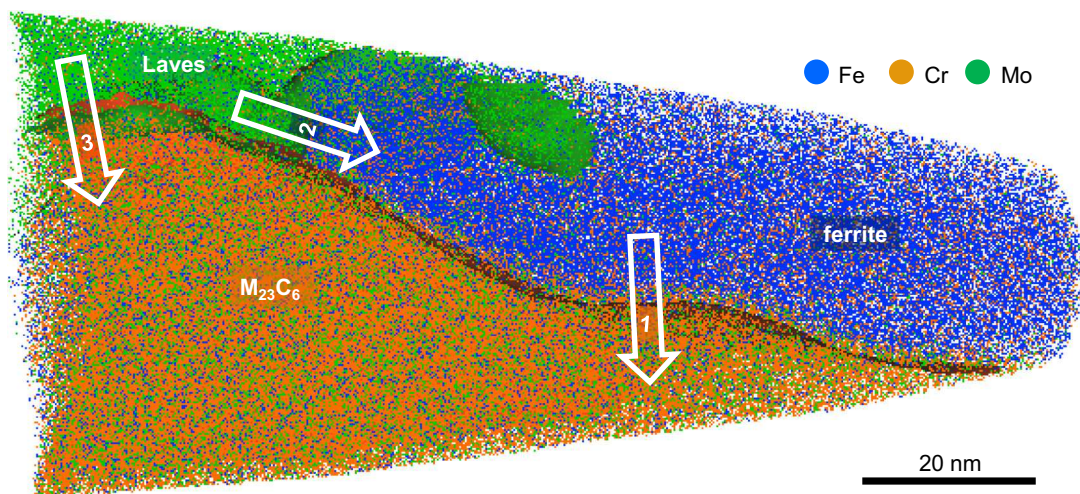


Fig. 9. Three dimensional distribution of atoms (Mo, green; Cr, orange; Fe, blue) in long-term crept specimen (material state L3b in Table 3). Violet, orange and green regions denote ferrite, $M_{23}C_6$ and Laves phase, respectively. White arrows mark the positions of the concentration profiles plotted in Fig. 10.

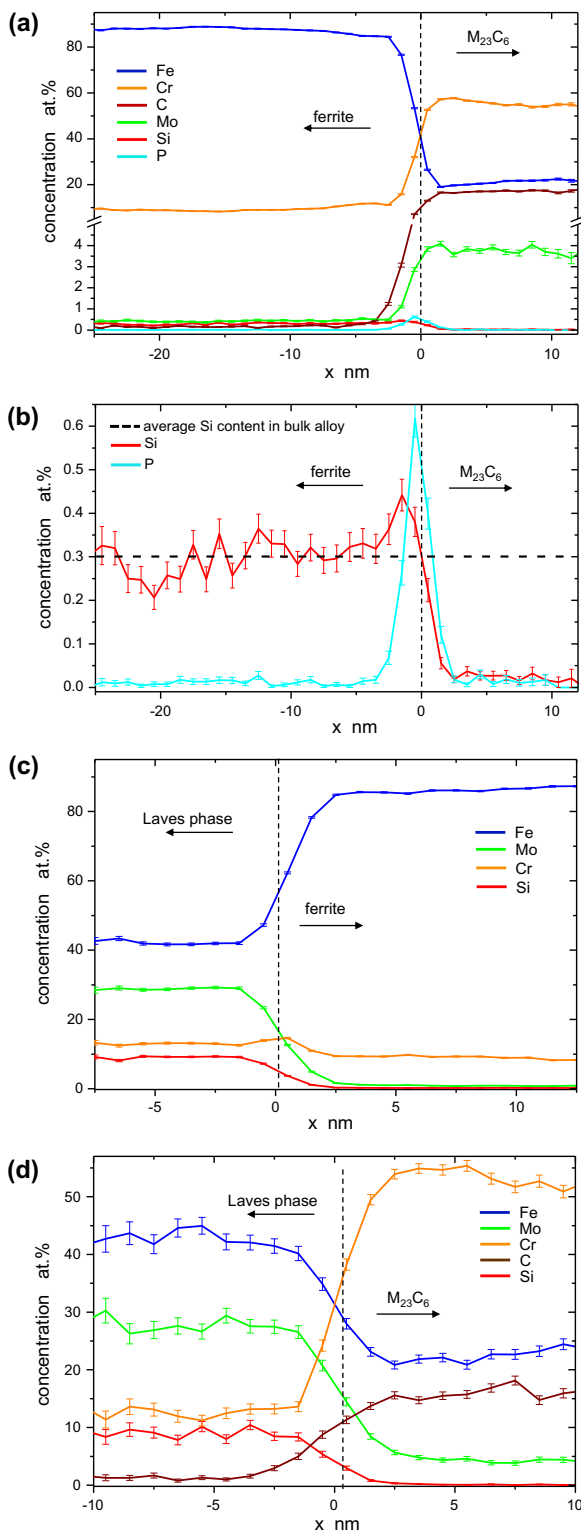


Fig. 10. Concentration profiles measured along the arrows in Fig. 9. (a) Distribution of the main elements, and (b) Si and P distribution across the ferrite/ $M_{23}C_6$ interface (both measured along the arrow 1 in Fig. 9 using an isoconcentration surface of 40 at.% Cr + C). (c) Concentration profile across the Laves phase/ferrite interface (measured along the arrow 2 in Fig. 9). (d) Concentration profile across the Laves phase/ $M_{23}C_6$ carbide interface (measured along the arrow 3 in Fig. 9). An isoconcentration surface of 20 at.% Mo + Si was used for both (c) and (d) plots.

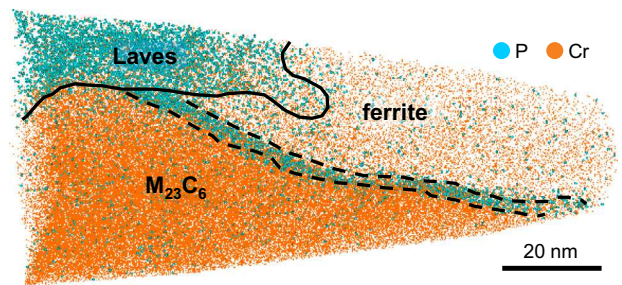


Fig. 11. Spatial distribution of Cr (orange dots) and P (cyan spheres) atoms in an APT tip prepared from long-term (81,984 h at 550 °C) crept specimen (material state L3b in Table 3).

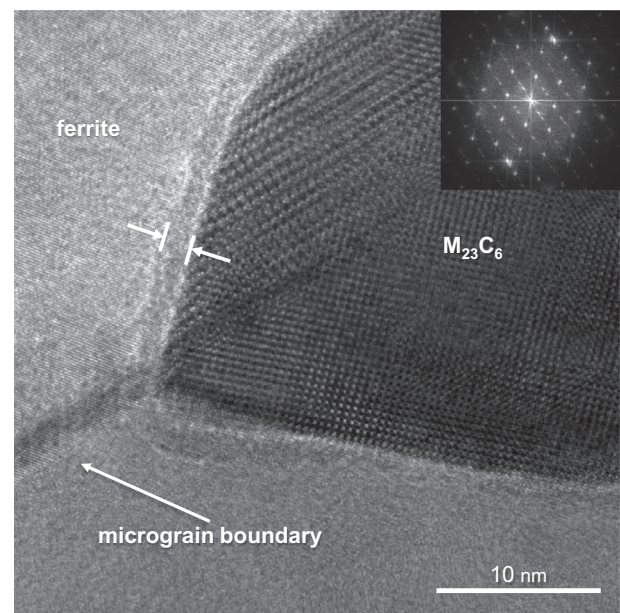


Fig. 12. High resolution TEM image of an $M_{23}C_6$ micrograin boundary carbide (material state L1a, shown in Table 3).

segregation of P to the ferrite/ $M_{23}C_6$ interface are clearly visible.

Fig. 12 shows a high resolution (HR) TEM micrograph of a $M_{23}C_6$ carbide on a micrograin boundary. The HR-TEM displays some important features. Firstly, it appears that the carbide shows different crystallographic orientations on both sides of the micrograin boundaries, which may be a result of its growth process. Secondly, the HR-TEM image qualitatively confirms the segregation results obtained by APT. The distinct contrast along the micrograin boundary and the carbide/ferrite interface (marked with arrows in Fig. 12) might be due to P segregation as quantified by the APT analysis (area marked with dashed lines in Fig. 11). Further work is required to clarify this point.

4. Discussion

TMFSs are important high temperature materials with complex microstructures which govern their mechanical

properties. The microstructure of TMFSs evolves during heat treatment and creep. Therefore, it is necessary to identify the elementary processes which govern this microstructural evolution, including the formation and growth of Laves phase particles. In earlier reports Mo, W, Nb and Ti rich Laves phase particles have been observed in TMFSs [11,25,28,42,59,71]. The present paper focuses on only the Mo-rich Laves phase particles [36,42,51,56,57,72]. Aghajani et al. [55] showed that Laves phase particles in X20CrMoV12-1 steel have a chemical composition close to 32 at.% Mo, 45 at.% Fe, 12 at.% Cr, 7 at.% Si and 1 at.% P. They proposed that the Laves phase particles can only nucleate and grow when this chemical equilibrium is established [55]. We propose that the differences in the thermodynamics and kinetics of nucleation and growth of Laves phase particles in different TMFSs are due to variations in the Si levels. Hosoi et al. and Kato et al. [51,73] studied the effect of Si on the precipitation of Laves phase and they showed that higher Si levels promote the formation of the Laves phase. Considering the presence of the Laves phase, there is a discrepancy between the thermodynamic predictions and experimental observations. Prior to heat treatment and creep no Laves phase is detected (Fig. 3) even though the MatCalc predicts Laves phase stability (Fig. 2). However, after high temperature exposure the formation of Laves phase particles has been observed (Figs. 4 and 5). Aghajani et al. [55] suggested that the slow diffusion of Si from the bulk matrix towards the Laves phase nuclei represents the rate-controlling step as the system strives towards thermodynamic equilibrium. Using analytical TEM and APT, we provided in Isik et al. [1] new information on the Laves phase nucleation and growth. Most importantly, we showed that segregation of Mo and Si to micrograin boundaries is required before the Laves phase can nucleate [1]. In the present study we explain why Laves phase particles are often observed not only on micrograin boundaries, but also next to $M_{23}C_6$ carbides [1,54,58]. Based on the present results (Figs. 4–6) we can exclude a direct transformation from a carbide to a Laves phase particle (as was suggested in [38]) and also the hypothesis that the phenomenon is closely related to Mo transfer from carbides to Laves phase particles (Figs. 6 and 10d). It was suggested in the literature [56] that Cr-depleted regions around carbides promote Laves phase nucleation, since they are enriched in Mo. However, we did not observe such high-Mo, low-Cr regions. The APT analyses of ferrite/ $M_{23}C_6$ interfaces in the initial state as well as after long-term creep (Figs. 7b and 10a) revealed that there is neither depletion in Cr nor enrichment in Mo. Instead, the results presented in Fig. 10c suggest that Laves phase nucleation does not require Cr depletion at internal interfaces.

Our results also suggest that there is one more factor that is critical for the Laves phase nucleation, which has been overlooked up to now. This is related to the fact that $M_{23}C_6$ carbides can accommodate only a limited concentration of Si, Tables 5 and 6. A negligible Si content was detected in the analyzed carbide observed in a specimen after 81984 h of creep (~ 9.3 years) at 550 °C (Table 6). Therefore, as these carbides nucleate and grow, they continuously reject Si atoms into the surrounding ferritic matrix and thus create a Si-rich environment in the ferrite, close to the ferrite/carbide interface (Figs. 8 and 10b). This thermodynamically promotes the nucleation of the Laves phase (Fig. 2b). It seems reasonable to assume that the

formation of Laves phase particles is promoted close to a carbide which pushes Si towards a micrograin boundary, where Si atoms from the matrix also segregate [1]. Our MatCalc estimates of the equilibrium compositions given in Table 2 suggest that, at equilibrium, carbides are Si free while Laves phase particles contain ~ 9 at.% Si. This is fully in line with our experimental findings.

A second factor identified in the present work is the role of phosphorus. P is observed in concentrations up to 1.3 at.% in the Laves phase particles, while it shows no solubility in carbides (Figs. 10b and 11). Moreover, P segregates at internal interfaces [74]. Thus, a Si- and P-rich environment surrounds the growing carbides and when these enhanced concentrations are rejected from the carbide, Laves phase nucleation occurs where the micrograin boundary is in contact with the carbide. Based on the results of the present study, we suggest that this is the reason why Laves phase particles form next to carbides at micrograin boundaries [1]. This phenomenon is summarized in the schematic illustration of Fig. 13. In Fig. 13a the formation of Mo, Si and P enriched regions is illustrated. The position where a micrograin boundary is in contact with a carbide appears to be a preferential nucleation site. As Fig. 13b suggests, Laves phase particles benefit from both, bulk segregation of Mo and Si to micrograin boundaries (as shown in Isik et al. [1]) and, in addition, by the Si and P enriched zones around growing carbides (present study).

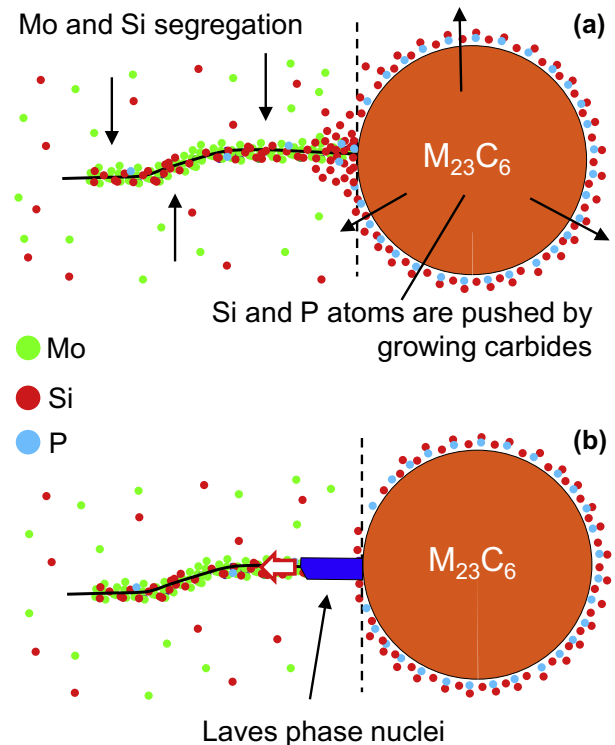


Fig. 13. Schematic summary of the role of carbides in assisting the Laves phase nucleation. (a) Formation of a Mo and Si enriched region on the micrograin boundary, while additionally Si and P atoms are pushed out of a carbide particle. (b) Nucleation of a Laves phase particle on the micrograin boundary in close vicinity to the carbide where the concentrations of Mo, Si and P are the highest (the red arrow denotes the growth direction).

The HR-TEM image shown in Fig. 12 suggests that the sharp corner of the $M_{23}C_6$ particle and associated local stress states (not discussed here) may also assist the Laves phase nucleation. Further work is required to clarify this aspect.

5. Summary and conclusions

The objective of the present work is to explain why Laves phase particles, which in previous studies were shown to nucleate at micrograin boundaries in tempered martensite ferritic steels, are often observed in the immediate vicinity of $M_{23}C_6$ carbides. Our results lead to the following conclusions:

- (1) The joint use of high resolution characterization methods such as HR-TEM and APT provides useful insight into the microstructural processes which govern the nucleation and growth of Laves phase particles.
- (2) For their nucleation and growth during high temperature exposure and creep, Laves phase particles require not only elevated Si but also elevated P levels (up to ~10 at.% and ~1.3 at.%, respectively), as compared to the average Si (~0.3 at.%) and P (~0.02 at.%) concentrations in these alloys. Local Si and P enrichments are required before Laves phase particles can form.
- (3) Two factors explain why Laves phase particles form next to micrograin boundary carbides: The segregation of Mo and Si to micrograin boundaries (detected previously in Isik et al. [1]), and the additional Si supply provided by Si enriched zones around growing carbides.
- (4) At carbide/ferrite interfaces a strong segregation of P was detected. This is related to the fact that carbides do not dissolve P and thus, as they nucleate and grow/coarsen, they push P into the ferrite matrix. This may further promote the formation of the Laves phase particles next to carbides.
- (5) There is a need for HR-TEM analyses to investigate the physical nature of carbides on micrograin boundaries. Their presence may well be associated with local stresses which can affect nucleation and also have an impact on the local micrograin boundary character.

Acknowledgements

The authors acknowledge funding through the International Max Planck Research School for Surface and Interface Engineering in Advanced Materials, IMPRS-SurMat. A.K. and G.E. acknowledge funding by the Max-Planck-Gesellschaft through the Max-Planck Fellow Group on High Temperature Materials at MPIE, Düsseldorf. The authors acknowledge support and fruitful discussions with E. Kozeschnik (TU Wien) and G. Inden.

References

- [1] M.I. Isik, A. Kostka, G. Eggeler, *Acta Mater.* 81 (2014) 230.
- [2] T. Fujita, *Advances in 9–12% Cr heat resistant steels for power plant*, in: R. Viswanathan, W.T. Bakker, J.D. Parker (Eds.), *Proceedings of the 3rd Conference on Advances in Material Technology for Power Plants*, The Institute of Materials, London, 2001.
- [3] A. Strang, M. McLean, *Modelling of Microstructural Evolution in Creep Resistant Materials*, The Institute of Materials, London, 1999.
- [4] M. Hättestrand, M. Schwind, H.O. Andren, *Mater. Sci. Eng. A250* (1998) 27.
- [5] N. Fujitsuna, M. Igarashi, F. Abe, *Key Eng. Mater.* 171–174 (2000) 469.
- [6] K. Maruyama, K. Sawada, J. Koike, *ISIJ Int.* 41 (2001) 641.
- [7] J. Pešička, A. Dronhofer, G. Eggeler, *Mater. Sci. Eng., A* 387–389 (2004) 176.
- [8] V. Sklenicka, K. Kucharova, M. Svoboda, L. Kloc, J. Bursik, A. Kroupa, *Mater. Charact.* 51 (2005) 35.
- [9] A. Kostka, K.G. Tak, R.J. Hellmig, Y. Estrin, G. Eggeler, *Acta Mater.* 55 (2007) 539.
- [10] A. Czyrska-Filemonowicz, A. Zielinska-Lipiec, P.J. Ennis, *J. Achiev. Mater. Manuf. Eng.* 19 (2006) 43.
- [11] K. Maile, *J. Int. Press Vessels Pip.* 84 (2007) 62.
- [12] K.G. Tak, U. Schulz, G. Eggeler, *Mater. Sci. Eng., A* 510–511 (2009) 121.
- [13] G. Eggeler, A. Dlouhy, *Z. Metallkd.* 96 (2005) 743.
- [14] D. Rojas, J. Garcia, O. Prat, L. Agudo, C. Carrasco, G. Sauthoff, A.R. Kaysser-Pyzalla, *Mater. Sci. Eng., A* 528 (2011) 1372.
- [15] P. Hu, W. Yan, W. Sha, W. Wang, Y. Shan, K. Yang, *J. Mater. Sci. Technol.* 27 (2011) 344.
- [16] N. Dudova, A. Plotnikova, D. Molodov, A. Belyakov, R. Kaibyshev, *Mater. Sci. Eng., A* 534 (2012) 632.
- [17] F. Liu, D.H.R. Fors, A. Golpayegani, H.O. Andren, G. Wahnström, *Metall. Mater. Trans. A* 43 (2012) 4053.
- [18] E.J. Payton, A. Aghajani, G. Eggeler, V.A. Yardley, *Scripta Mater.* 66 (2012) 1045.
- [19] J. Pešička, A. Aghajani, C. Somsen, A. Hartmaier, G. Eggeler, *Scripta Mater.* 62 (2010) 353.
- [20] P.J. Szabo, *Mater. Sci. Eng., A* 387–389 (2004) 710.
- [21] Q. Wu, *Microstructural Evolution in Advanced Boiler Materials for Ultra-Supercritical Coal Power Plants*, University of Cincinnati, Cincinnati, 2006.
- [22] G.B. Olson, *Mater. Sci. Eng., A* 273 (1999) 11.
- [23] A. Dronhofer, J. Pešička, A. Dlouhy, G. Eggeler, *Z. Metallkd.* 94 (2003) 511.
- [24] A. Aghajani, (Dr.-Ing thesis), Cuvillier Verlag Göttingen, Bochum, 2009.
- [25] G. Eggeler, *Acta Metall.* 37 (1989) 3225.
- [26] G. Eggeler, J.C. Earthman, N. Nilsvang, B. Ilschner, *Acta Metall.* 37 (1989) 49.
- [27] G. Eggeler, N. Nilsvang, B. Ilschner, *Steel Res.* 2 (1987) 97.
- [28] A. Aghajani, C. Somsen, G. Eggeler, *Acta Mater.* 57 (17) (2009) 5093.
- [29] F. Abe, T.U. Kern, R. Viswanathan, *Creep-Resistant Steels*, Woodhead Publishing, CRC Press, Cambridge, 2008.
- [30] R. Bürgel, H.J. Maier, T. Niendorf, *Handbuch Hochtemperatur-Werkstofftechnik*, Vieweg Teubner Verlag Springer Fachmedien Wiesbaden GmbH, Wiesbaden, 2011.
- [31] J. Cadek, *Creep in Metallic Materials*, Elsevier, Amsterdam, 1988.
- [32] R.W. Evans, B. Wilshire, *Creep of Metals and Alloys*, Institute of Metals, London, 1985.
- [33] J.D. Robson, H.K.D.H. Bhadeshia, *Mater. Sci. Technol.* 13 (1997) 631.
- [34] J.D. Robson, H.K.D.H. Bhadeshia, *Mater. Sci. Technol.* 13 (1997) 640.
- [35] C. Wiesner, J.C. Earthman, G. Eggeler, B. Ilschner, *Acta Metall.* 37 (1989) 2733.
- [36] T. Fujita, N. Takahashi, *ISIJ Trans.* 18 (1978) 703.
- [37] L.M. Lundin, *Scripta Mater.* 34 (1996) 741.
- [38] Y. Tsuchida, K. Okamoto, Y. Tokunaga, *ISIJ Int.* 35 (1995) 317.
- [39] A. Dronhofer, J. Pešička, G. Eggeler, *J. Phys. IV France* 11 (Pr8-23) (2001) 5.
- [40] V. Foldyna, Z. Kuboň, A. Jakobová, V. Vodárek, *Development of advanced high chromium ferritic steels*, in: A. Strang, D.J. Gooch (Eds.), *Microstructural Development and Stability in High Chromium Ferritic Power Plant Steels*, The Institute of Materials, London, 1997.
- [41] H. Cui, F. Sun, K. Chen, L. Zhang, R. Wan, A. Shan, J. Wu, *Mater. Sci. Eng., A* 527 (2010) 7505.

- [42] A. Kipelova, A. Belyakov, R. Kaibyshev, *Mater. Sci. Eng.*, A 532 (2012) 71.
- [43] P.J. Ennis, A. Czyrska-Filemonowicz, *Sadhana* 28 (2003) 709.
- [44] J. Hald, *J. Int. Press Vessels Pip.* 85 (2008) 30.
- [45] D. Rojas, J. Garcia, O. Prat, C. Carrasco, G. Sauthoff, A.R. Kaysser-Pyzalla, *Mater. Sci. Eng.*, A 527 (2010) 5976.
- [46] S. Yamasaki, (PhD thesis), Cambridge, 2004.
- [47] J. Vanaja, K. Laha, R. Mythili, K.S. Chandravathi, S. Saroja, M.D. Mathew, *Mater. Sci. Eng.*, A 533 (2012) 17.
- [48] B.S. Srinivas-Prasad, V.B. Rajkumar, K.C. Hari-Kumar, *CALPHAD* 36 (2012) 1.
- [49] E. Kozeschnik, J. Svoboda, F.D. Fischer, *CALPHAD* 28 (2004) 379.
- [50] MatCalc, The Materials Calculator Software. <<http://matcalc.tuwien.ac.at/>>.
- [51] Y. Hosoi, N. Wade, S. Kunimitsu, T. Urita, *J. Nucl. Mater.* 141–143 (1986) 461.
- [52] K. Miyahara, J.H. Hwang, Y. Shimoide, *Scripta Metall. Mater.* 32 (1995) 1917.
- [53] M. Svoboda, A. Dlouhy, I. Podstranska, V. Sklenicka, K.H. Mayer, in: *Int. Conf. Metall. Mater.*, Brno, Czech Republic, 15–17 May, 2013.
- [54] I. Fedorova, A. Kipelova, A. Belyakov, R. Kaibyshev, *Metall. Mater. Trans. A* 44A (2013) 128.
- [55] A. Aghajani, F. Richter, C. Somsen, S.G. Fries, I. Steinbach, G. Eggeler, *Scripta Mater.* 61 (2009) 1068.
- [56] B.A. Senior, *Mater. Sci. Eng. A* 119 (1989) 5.
- [57] K. Sawada, M. Takeda, K. Maruyama, R. Ishii, M. Yamada, Y. Nagae, R. Komine, *Mater. Sci. Eng.*, A 267 (1999) 19.
- [58] O. Prat, J. Garcia, D. Rojas, G. Sauthoff, G. Inden, *Intermetallics* 32 (2013) 362.
- [59] I. Fedorova, A. Belyakov, P. Kozlov, V. Skorobogatykh, I. Shenkova, R. Kaibyshev, *Mater. Sci. Eng.*, A 615 (2014) 153.
- [60] M.K. Miller, K.F. Russell, K. Thompson, R. Alvis, D.J. Larson, *Microsc. Microanal.* 13 (2007) 428.
- [61] P. Felfel, S. Ringer, J. Cairney, *Ultramicroscopy* 111 (2011) 435.
- [62] S. Mandal, K.G. Pradeep, S. Zaefferer, D. Raabe, *Scripta Mater.* 81 (2014) 16.
- [63] L. Yuan, D. Ponge, J. Wittig, P. Choi, J.A. Jimenez, D. Raabe, *Acta Mater.* 60 (2012) 2790.
- [64] Integrated Visualization and Analysis Software (IVAS) for Atom Probe, Cameca Instr, <<http://www.cameca.com/>>.
- [65] L. Kaufman, H. Bernstein, *Computer Calculation of Phase Diagrams*, Academic Press, New York, 1970.
- [66] L. Kaufman, *CALPHAD – Computer Coupling of Phase Diagrams and Thermochemistry*, Pergamon, Oxford, 1977.
- [67] B. Sundman, B. Jansson, J.O. Andersson, *CALPHAD* 9 (1985) 153.
- [68] N. Saunders, P. Miodownik, *CALPHAD: Calculation of Phase Diagrams*, Pergamon, 1998.
- [69] H. Lukas, S.G. Fries, B. Sundman, *Computational Thermodynamics: The CALPHAD Method*, Cambridge Univ Press, 2007.
- [70] P.J. Spencer, *CALPHAD* 32 (2008) 1.
- [71] K. Yamamoto, Y. Kimura, Y. Mishima, *ISIJ Int.* 43 (2003) 1253.
- [72] N. Fujita, K. Ohmura, A. Yamamoto, *Mater. Sci. Eng.*, A A351 (2003) 272.
- [73] Y. Kato, M. Ito, Y. Kato, O. Furukimi, *Mater. Trans.* 51 (2010) 1531.
- [74] D. Raabe, S. Sandloebes, J. Millan, D. Ponge, H. Assadi, M. Herbig, P.P. Choi, *Acta Mater.* 61 (2013) 6132.